ARTICLE

Check for updates

Hybrid microstructure of smectite clay gels revealed using neutron and synchrotron X-ray scattering

Mohammad Shoaib[1,2 ✉], Shaihroz Khan [1], Omar B. Wani [1], Jitendra Mata [3,4], Anthony J. Krzysko[5], Ivan Kuzmenko[5], Markus Bleuel[6,7], Lindsey K. Fiddes[8], Eric W. Roth[9] & Erin R. Bobicki[1,10 ✉]

Aqueous suspensions of swelling clays display a nematic sol-gel transition at very low solid concentrations. The underlying microstructure of the gel has remained a point of contention since the time of Irving Langmuir and has been a major obstacle to fully realizing the potential of clays for practical applications. Here, we comprehensively probe the microstructure of a smectite clay suspension using ultra-small angle neutron/X-ray scattering and find that the nematic gel is structurally ordered and contains entities that are at least an order of magnitude larger than the individual particles. Complementary cryo-electron microscopy shows the presence of domains having particle-particle ordering responsible for nematic texture and regions of particle-particle aggregation responsible for gel-like behavior. We find that the smectic clay gels have a hybrid microstructure with co-existing repulsive nematic domains and attractive disordered domains.

[1] Department of Chemical Engineering and Applied Chemistry, University of Toronto, Toronto, ON M5S 3E5, Canada. [2] Earth and Environmental Sciences Area, Lawrence Berkeley National Laboratory, 1 Cyclotron Rd., Berkeley, CA 94720, USA. [3] Australian Centre for Neutron Scattering (ACNS), Australian Nuclear Science and Technology Organisation (ANSTO), Lucas Heights, Sydney, NSW 2232, Australia. [4] School of Chemistry, University of New South Wales, Sydney, NSW 2052, Australia. [5] Argonne National Laboratory, 9700S. Cass Avenue, Bldg. 433A, Argonne, IL 60439, USA. [6] NIST Center for Neutron Research, National Institute of Standards and Technology, Gaithersburg, MD 20899, USA. [7] Department of Materials Science and Engineering University of Maryland College Park, College Park, MD 20742-2115, USA. [8] Temerty Faculty of Medicine, University of Toronto, Toronto, ON, Canada. [9] Northwestern University Atomic and Nanoscale Characterization Experimental Center, Northwestern University, 2220 Campus Drive, Evanston, IL 60208, USA. [10] Chemical and Materials Engineering Department, University of Alberta, Edmonton, Canada. ✉email: mohammad.shoaib@mail.utoronto.ca; bobicki@ualberta.ca

Clays are naturally occurring phyllosilicate minerals that play an important role in natural processes like debris flows, transport and fate of nutrients in the lithosphere and in industrial systems including drilling, paper making, nuclear waste disposal, health and beauty product manufacturing, and mineral processing[1–5]. Clays are classified as swelling and non-swelling types based on the delamination capability of thick clay sheets into individual layers or not. The colloidal behavior of swelling types of clays such as smectite and hectorite has been the subject of numerous studies dating back to the seminal work of Irving Langmuir and Herbert Freundlich[6,7]. The structures of these clays consist of dioctahedral aluminium hydroxide, or trioctahedral magnesium hydroxide sheets sandwiched between two tetrahedral silica sheets (Fig. 1a). Isomorphic substitutions by less charged cations produce a net negative layer charge in octahedral and tetrahedral layers that is compensated by the interlayer cations that control both swelling and colloidal behaviour of sodium-montmorillonite (Na-Mt) suspensions (Fig. 1b)[8–11]. Montmorillonites have different chemistries arising due to different extents of octahedral isomorphic substitution that directly impact the physicochemical or microscopic and macroscopic properties of montmorillonite suspensions. As an example, the cation exchange capacity (CEC) of Swy-3 montmorillonite (96 meq per 100 g) is lower than that of SAz-1 montmorillonite (120 meq per 100 g) attributed to a greater isomorphic substitution (Al→Mg) in SAz-1[12] compared to Swy-3 resulting in slightly different colloidal behaviour of the two montmorillonites.

Unlike suspensions of swelling clays such as nontronite (NAu-1), nontronite (Nau-2), and beidellite (SBId-1) that display a clear entropy-driven, first-order isotropic to nematic transition[13–17], the aqueous suspensions of Na-Mt smectite clay display a nematic sol-gel transition at very low volume fractions[18]. The existence of gelation prevents suspensions from reaching a true thermodynamic equilibrium[19,20]. The microstructure of the gel has remained a point of contention in the literature. Two models, repulsive or attractive have been proposed based on the overall particle-particle interactions being either repulsive or attractive. The repulsive model predicts an oriented network stabilized by repulsive forces caused by interacting double layers (Fig. 1c)[12,21–25] supported by the fact that the sol state exhibits a shear-induced optical birefringence that disappears once shearing is stopped, and the gel state remains permanently birefringent[26] with the development of a yield stress

and a smectic or poorly crystalline microstructure. As a result, the development of yield stress in the repulsive model is attributed to a repulsive jamming transition rather than a percolation threshold. Conversely, the attractive model assumes the formation of a tri-dimensional network governed by electrostatic attraction between platelets supported by the development of yield stress or jamming at very low solids concentrations (Fig. 1d)[27,28] attributed to the attractive particle-particle interaction.

Furthermore, the attractive model above is also supported by the fact that, even in the sol state, the shear-induced ordering transition occurs at very low Peclet numbers (Pe) based on the size of individual particles (Pe $\sim a^3$, where a is the particle diameter)[29]. At these low Peclet numbers, the particles should not be oriented and should be randomly organized. The time required for shear-induced ordering to disappear when the shear stress is removed is longer than the rotational time of a single particle[30]. Moreover, the number density of particles required for the sol-gel transition evolves as the inverse of the average particle diameter, suggesting that the entities that remain at the origin of the sol-gel transition are clusters or stacks, not individual particles[31].

After several decades of rigorous research, the precise microstructure of Na-Mt gels remains elusive. Although DLVO (Derjaguin, Landau, Vervey, and Overbeek) theory has played a major role in our understanding of colloidal suspensions, its applicability to swelling clay suspensions—similar to the case of cement where the DLVO theory does not predict any cohesion[32,33]—is debated due to possible contributions of long-range attraction between like-charged particles amongst the other possible reasons[34–37]. Further, the issue is not fully resolved from a theoretical point of view[38,39]. Furthermore, Batista et al.[40] highlighted the nonadditivity of electrostatic, van der Waals and other interactions in suspensions of nanoparticles especially <100 nm resulting in the breakdown of DLVO theory to understand the interaction in nano-suspensions. The unfractionated Na-Mt suspensions are a mix of particles with a size range from ~20–600 nm, therefore, due to the nonadditivity of interactions, the application of DLVO to understand this system is rather challenging. Previous studies have either been limited by the minimum scattering angle, which can only cover a length scale up to 1 μm, or they have relied on rheology to discern the microstructure. A more robust method would probe the microstructure at length scales much larger than individual particles, which
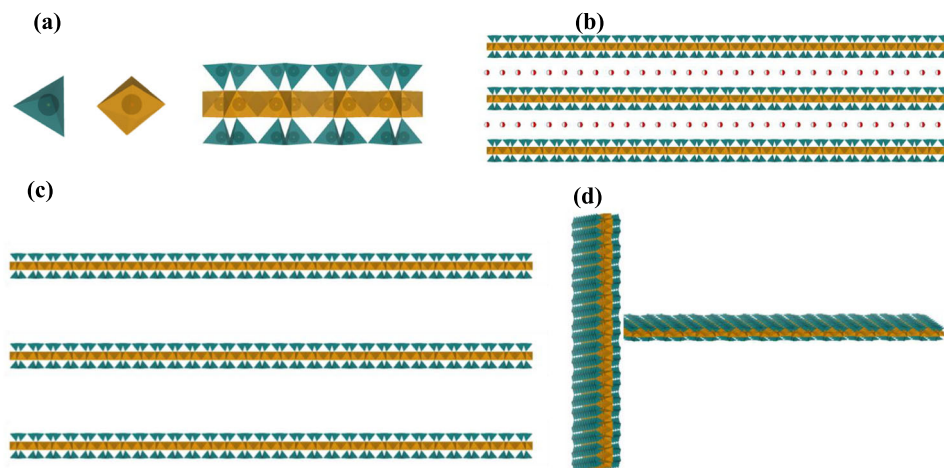

Fig. 1 Overview of sodium-montmorillonite (Na-Mt) structure and proposed microstructures in literature. a Silica tetrahedra and alumina octahedra that form the basis of Na-Mt structure with alumina octahedral sheet sandwiched between two silica tetrahedral sheets. **b** Tactoids of Na-Mt sheets in dry form with intercalated cations that compensate for the layer charge that arises due to the isomorphous substitution. **c** The tactoids delaminate or swell to make a suspension stabilized by repulsive double-layer repulsions between particles giving rise to a repulsive microstructure that is optically birefringent or anisotropic. **d** The particles aggregate due to an attractive interaction between edge and basal plane giving rise to an attractive microstructure.
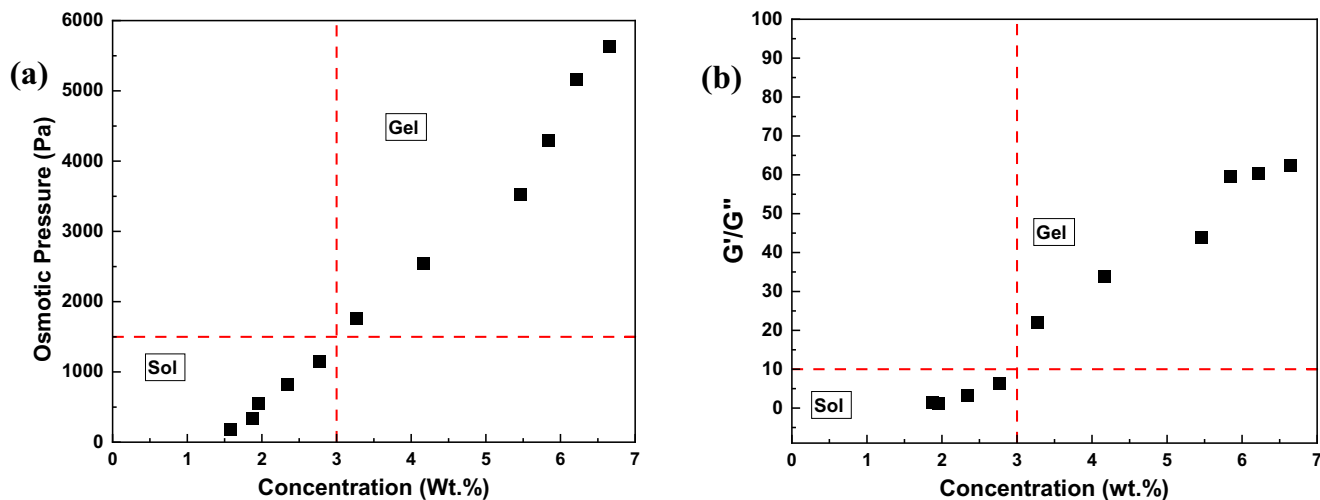
Fig. 2 Osmotic pressure and rheological properties. a Osmotic pressure vs Swy-3 Na-Mt suspension concentration, **b** ratio of storage modulus (G') to loss modulus (G") for Na-Mt suspensions in the sol and gel states.

requires the ability to measure very small angles[41]. Here, we probe the microstructure of Na-Mt suspensions below and above the gel point using ultra-small angle X-ray scattering (USAXS) and ultra-small angle neutron scattering (USANS) along with high-pressure cryogenic scanning electron microscopy (cryo-SEM), cryogenic transmission electron microscopy (cryo-TEM), and dilution studies on ultra-low ionic strength (10^{-5} M) Swy-3 Na-Mt suspensions.

Results

The osmotic pressure of Na-Mt suspensions increased gradually as a function of concentration in the sol state (Fig. 2a). Osmotic pressure in the sol state increased linearly until ~10^3 Pa (3 wt% concentration). In the gel state, the osmotic pressure increased exponentially signifying the difference between sol and gel states as well as the higher pressures required to concentrate the suspensions in the gel state. Osmotic pressure represents the force resisting the extraction of liquid. It originates from an increase in energy (interparticle forces) and/or a loss of entropy (configurations)[42,43]. The increase in the pressure required to reach concentrations above 3 wt% signifies enhanced interparticle forces in the gel state. These results are similar to the results reported in other studies on Na-Mt systems[12,26].

The ratio of the linear viscoelastic storage modulus (G') to loss modulus (G") was below 10 in the sol state and above 10 beyond the gel point (Fig. 2b). Similar to osmotic pressure, the ratio increased gradually as a function of concentration in the sol state, but unlike osmotic pressure, the ratio increased more gradually with increasing Na-Mt concentration in the gel state. In the gel state, G' evolves exponentially similar to the osmotic pressure indicating a common underlying mechanism responsible for osmotic pressure and G' in Na-Mt suspensions (Supplementary Figure 1a). The G' acquires values of the order of 10^3 Pa at higher concentrations signifying a very high strength of the gelled microstructure (Supplementary Figure 1a). Similar results are also obtained for Na-Mt in deuterium oxide (D_2O) except that the gel point is achieved at a lower Na-Mt weight concentration in the presence of D_2O due to the density difference between D_2O and water which meant a higher volume fraction of Na-Mt at the same weight concentration (Supplementary Figure 1b, c).

When viewed between crossed polarizers, Na-Mt suspensions in the sol state remained optically isotropic and only briefly exhibited birefringence immediately after being sheared (Fig. 3a), whereas, in the gel state, they exhibited a permanent birefringence

or nematic character (Fig. 3b, c). The time required for the shear-induced birefringence to disappear increased as a function of concentration in the sol state until the system "locked" the particles or entity responsible for the nematic character at the gel point. Therefore, the sol and gel states both exhibited ordering. For the sol state, an external shear was required for the ordering to be evident, and for the gel state, a mechanism was needed through which the shear-induced effect could be retained. Therefore, the relaxation time—the time required for the microstructure to transition from order to disorder—was very short in the sol state and very long in the gel state[30]. This shear-induced and permanent birefringence has also been observed in aqueous suspensions of other geometrically anisotropic particles (e.g., laponite and cellulosic nanocrystal)[30,44]. The main question is how the driving force differs between the shear-induced ordering in the sol state and the permanent ordering in the gel state. It is also worth mentioning that the gel behaviour in D_2O appears at a concentration lower than accounted by the density difference, at a volume/volume concentration of ~1% in the case of D_2O as compared to ~1.30% in H_2O. These differences could be due to 20% higher viscosity of D_2O compared to H_2O at 25 °C[45,46].

Ultra-small-angle X-ray scattering (USAXS). The slope of the intensity versus scattering wave vector (Q) curve was approximately –2 (Fig. 4a, b), signifying the nearly bi-dimensional nature of the disks[15,47]. The USAXS data at the lowest Q values in the sol state can be seen to be hardly flattening up at the lowest three concentrations and takes an upturn above 2.3 wt% concentration. From this concentration onward, the slope of the curve at the lowest Q values increases significantly which suggests the entities grow as a function of concentration[48–51]. Therefore, the USAXS results provided the proof that entities much larger than ~6 μm are present in Na-Mt suspensions. Further, a "bump" in the vicinity of 10^{-2} Å^{-1}, which is more visible when $Q^2 I$ is potted against Q (Fig. 4c, d), corresponds to the short-range positional order of the platelets or characteristic repeat distance in the underlying microstructure. This has been provided as evidence of a purely repulsive microstructure in Na-Mt suspensions[12,52]. However, our results clearly show that there is much to the microstructure beyond the length scale where this ordering is observed. Therefore, the bump may correspond to the short-range positional order of one type of platelets that are smaller. A second bump in the curve at 4×10^{-4} Å^{-1} (~1.5 μm) may be the
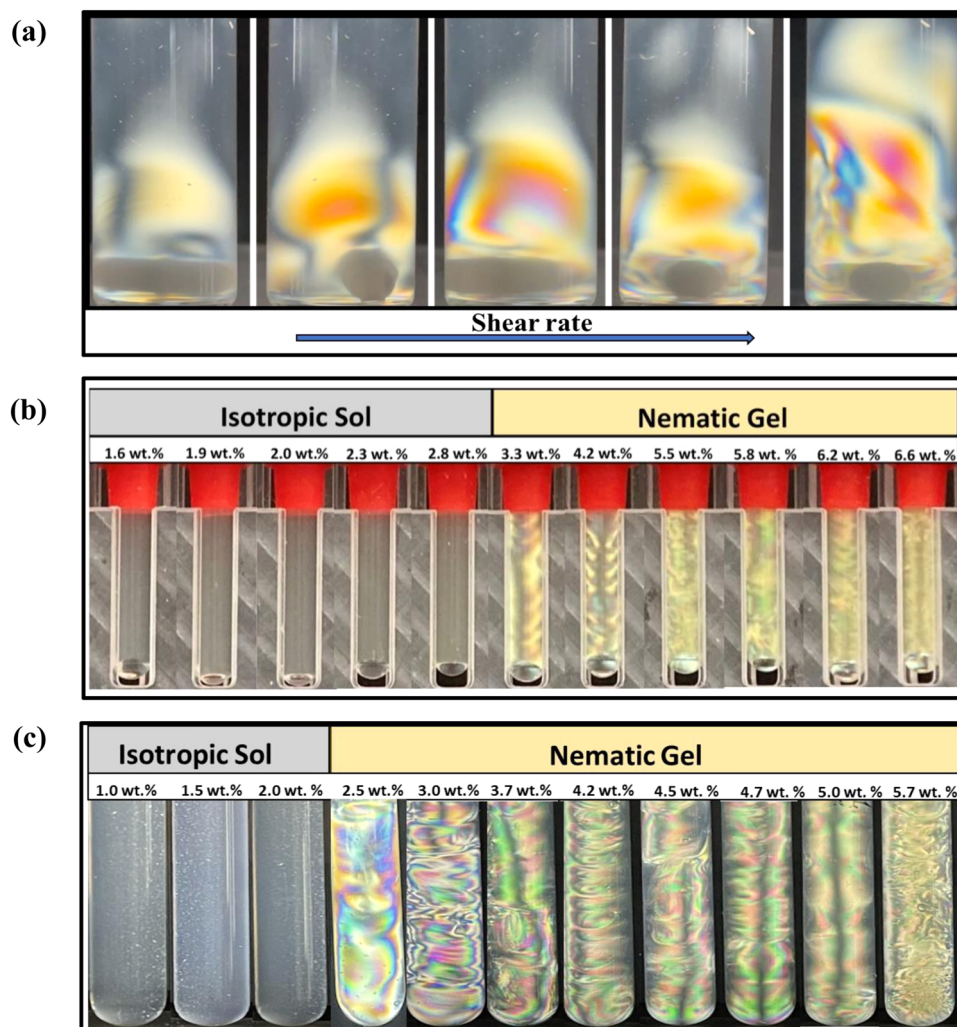
Fig. 3 Visual observation of Na-Mt suspensions in the sol and gel states between crossed polarizers. a Shear-induced birefringence in the sol state of Na-Mt suspensions (1.6 wt%), the birefringence grows as the shear rate is increased signifying enhanced ordering at higher shear rates; visualizations of Na-Mt suspensions **b** in H_2O and **c** in Deuterium oxide (D_2O), in the sol and gel states between crossed polarizers. Note that the birefringent pattern evolves as a function of concentration in the gel state. The gel point is between Na-Mt concentration 2.8–3.3 wt% in H_2O and between 2.0–2.5 wt% in D_2O.

distance between aggregated entities composed of several larger particles or between the repulsive nematic domains which is not impacted by concentration greatly. The microstructure can then be viewed as hybrid, containing segregated domains of ordered particles responsible for birefringence and aggregated particles responsible for gelation. Therefore, the microstructure of Na-Mt suspensions is complex rather than simply repulsive or attractive.

The osmotic pressure decayed exponentially as a function of the average interparticle distance obtained from the length scale at the maximum oscillation of the scattering intensity ($2\pi/Q$). The reduced osmotic pressure ($P_{osm}/4 \times C_{salt}RT$, Where P_{osm} is the Osmotic Pressure, C_{salt} is the salt concentration, R is the Universal gas constant, and T is the temperature) plotted against the interparticle distance normalized to Debye length fell close to the analytical solution of the Poisson-Boltzmann equation solved for a symmetrical 1:1 electrolyte for two parallel infinite plates at separation distances >>0.64 nm[12,31] (Fig. 4e). These results are similar to those reported for Swy-2 montmorillonite based on small-angle X-ray scattering[12] and signify the role of repulsive electrostatic interactions in the microstructure. It is worth noting that a permanent birefringence pattern develops when the interparticle separation is equivalent to the Debye length ($d/k^{-1} \sim 1$), further confirming the role of electrical double-layer interactions in the microstructure. Swelling law relating the interparticle distance to volume fraction approximately follows a unidimensional swelling for which the average thickness of the individual particles is obtained by $D = t\varphi^{-1}$, where t is the layer thickness[12,15,53] (Fig. 4f). The slope of the line suggests the platelet thickness of particles responsible for the diffuse peak is ~1 nm, which is close to the thickness of a single clay sheet[12].

Microstructure evolution monitored over three months of aging with USAXS did not show any dramatic variation, apart from minute changes signifying very slow structural changes. These include enhanced aggregation as reflected by the extreme upturn in the scattering intensity at the lowest scattering angles at high Na-Mt concentrations in the gel state (Supplementary Figure 2b) and a smaller interparticle distance in the aged (3 months sample) than fresh system (3 days sample) (Fig. 4e). The aging results thus indicate that the Na-Mt suspensions were out of equilibrium and additional study focusing on this aspect using advanced techniques such as X-ray photon correlation spectroscopy is warranted.

The SAXS profiles for sol and gel states were similar with intensity decaying at a slope of ~−2 till Q values of around 0.2 Å^{-1} (Supplementary Figure 3). The SAXS region also didn't have a peak in the vicinity of 0.1 Å^{-1} which typically represents the presence of tactoids in Na-Mt suspensions[54]. The aging of samples didn't
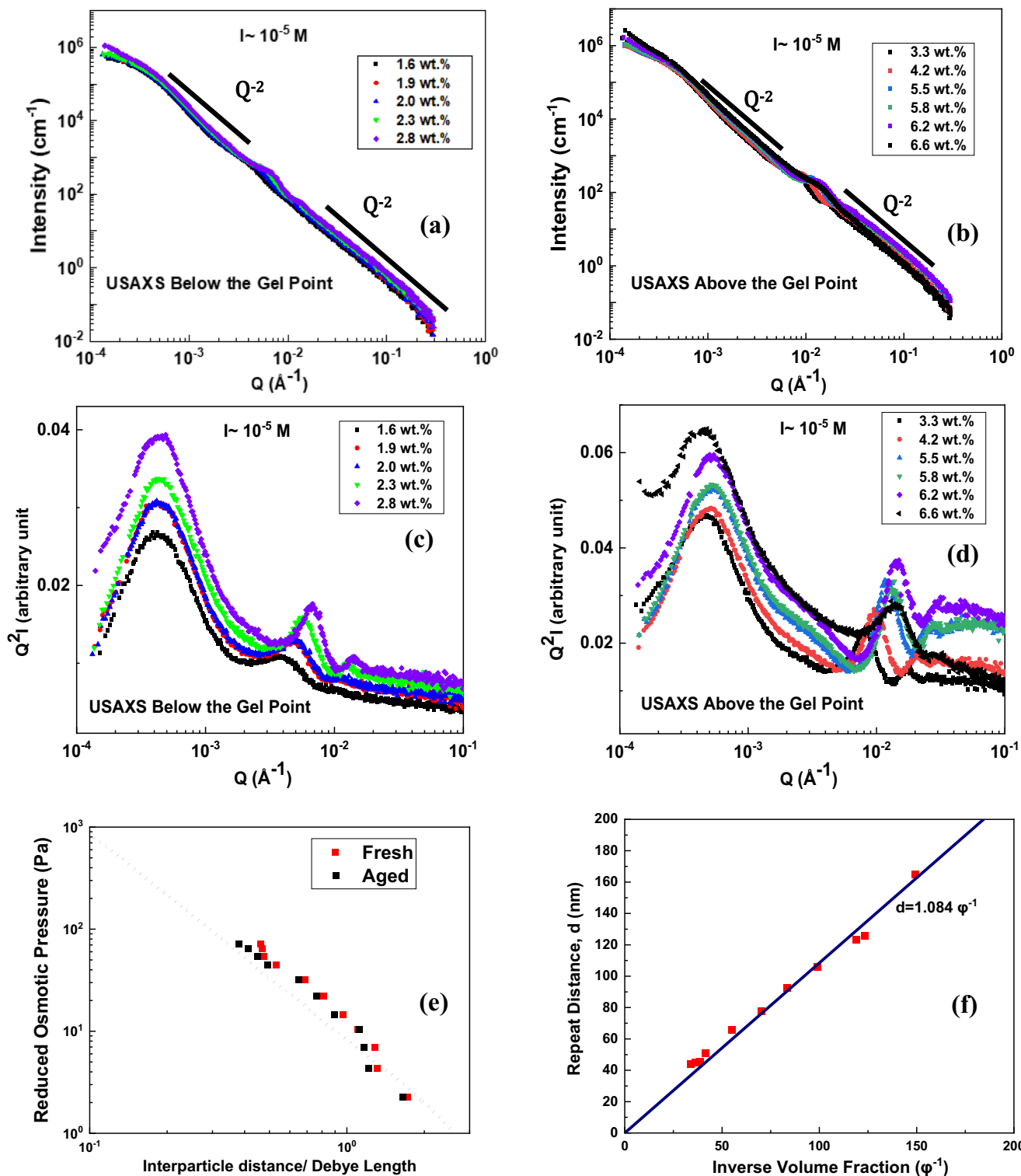
Fig. 4 X-ray scattering of Na-montmorillonite aqueous suspensions. Ultra-small angle X-ray scattering analysis of low ionic strength (10^{-5} M) sodium-montmorillonite suspensions **a**, **c** in the sol state and **b**, **d** in the gel state; **e** reduced osmotic pressure vs interparticle distance scaled to Debye length; dashed line represents the asymptotic solution of eq A6 in the ref. [31] with $\sigma = -0.11$ C·m^{-2} and H $\gg$ 0.3 nm for a symmetrical 1:1 electrolyte solution given by $\frac{H}{L_D} = \sqrt{\frac{1}{1+P^*}} K\left(\frac{1}{1+P^*}\right)$ where P^* is the reduced osmotic pressure and K is the is the complete elliptic integral of the first kind; and **f** evolution of repeat distance between particles vs inverse volume fraction.

influence the SAXS profile significantly (Supplementary Figure 4). Similarly, WAXS region scattering for both the fresh and aged samples were also similar suggesting the crystal structure of the sample remained intact (Supplementary Figures 3 and 4).

Ultra small angle neutron scattering (USANS). After confirming the presence of objects much larger than the scale covered by USAXS, we probed the length scale of the entities up to 17 μm using USANS. Both the sol (Fig. 5a) and gel states (Fig. 5b) exhibited
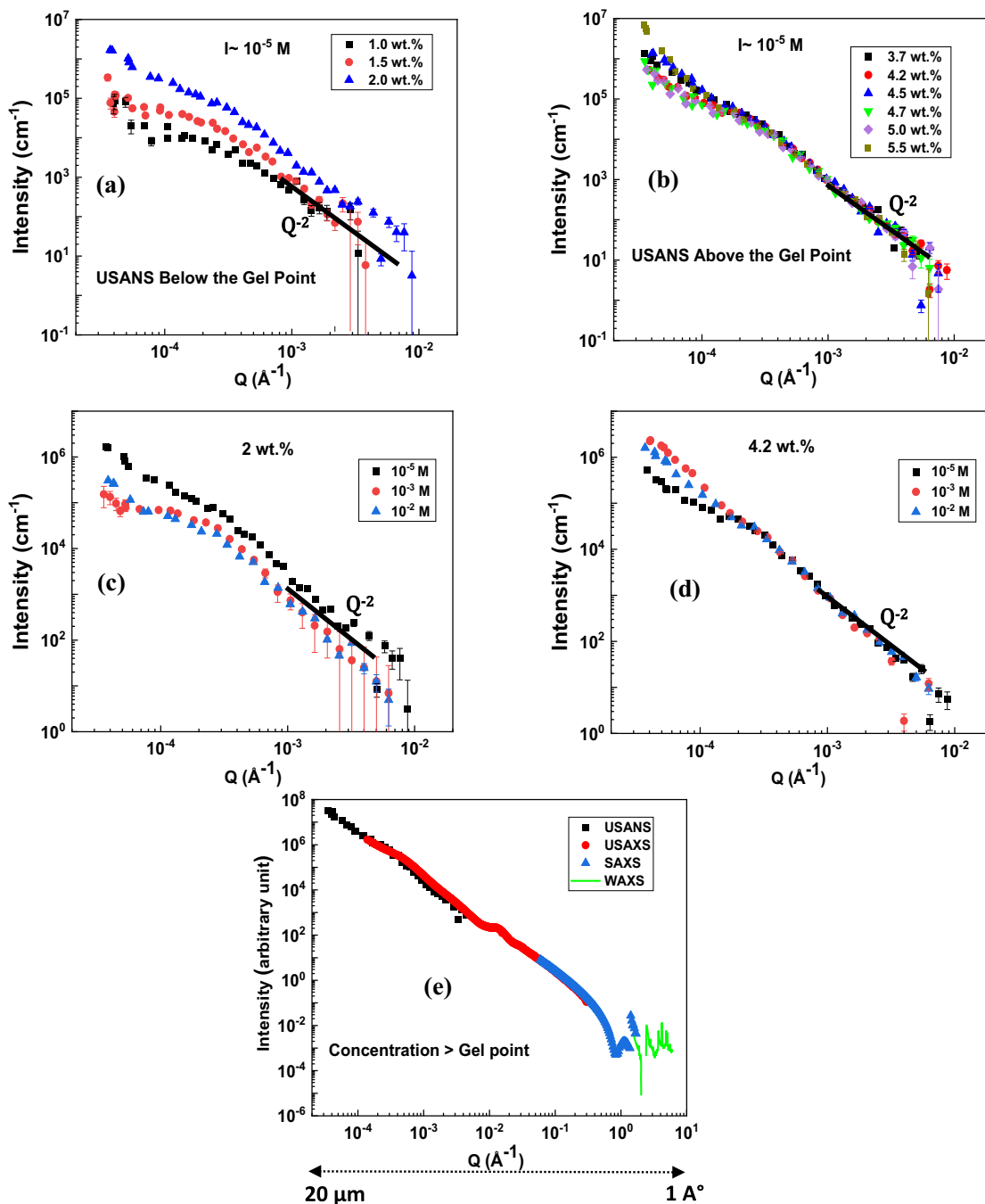
Fig. 5 Neutron scattering of Na-montmorillonite aqueous suspensions. a Ultra-small angle neutron scattering (USANS) of low ionic strength (10^{-5} M) Swy-3 sodium-montmorillonite (Na-Mt) suspensions in the sol state and **b** in the gel state; representative USANS data for Na-Mt suspensions **c** in the sol state and **d** in the gel state at three ionic strengths; and **e** combined scattering data from wide (WAXS), small (SAXS), and ultra-small angle scattering (USAXS) and USANS in the gel state at 6.2 wt% concentration. The error bars in (**a**), (**b**), (**c**), and (**d**) represent the standard deviations calculated from counting statistics.

scattering at the lowest scattering angles, indicating the presence of entities much larger than 17 μm[50]. The slope of the intensity vs. Q curve increased with concentration in both states, showing that aggregation of Na-Mt suspensions increased in extent with increasing concentration. These results further clarify the microstructure of Na-Mt suspensions and contradict a purely repulsive microstructure.

The effect of ionic strength on the microstructure was also studied with USANS. For the sol state, the introduction of salt resulted in a counterintuitive reduction in intensity but scattering at the lowest Q was similar regardless of the ionic strength, signifying aggregation

(Fig. 5c). For the gel state, increasing ionic strength increased the intensity, signifying intensified aggregation in the presence of salt (Fig. 5d). The USAXS and USANS scattering data in the gel state covering a length scale of 1 Å to 17 μm overlapped, albeit with a slight vertical shift to account for the intensity difference between the two methods (Fig. 5e). The bending in the scattering curve around a Q of 4×10^{-4} Å^{-1} was consistent for both USAXS and USANS.

High-pressure Cryo-SEM and Cryo-TEM. The sol state exhibited few contacts between particles without any ordering (Fig. 6a, c),
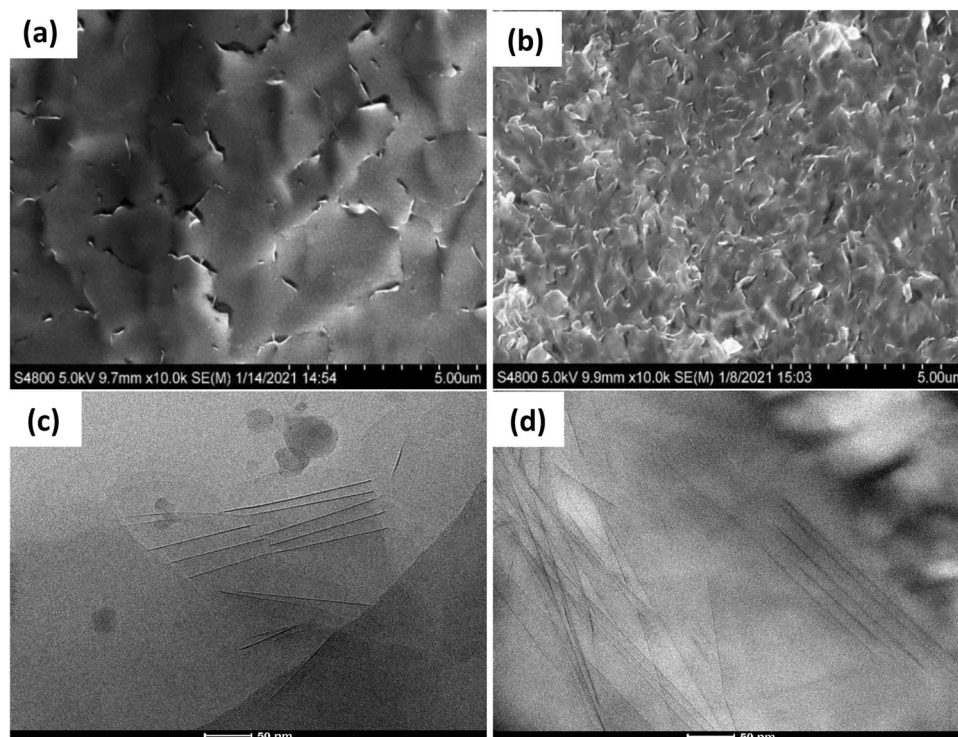
Fig. 6 Cryo-Electron Microscopy in sol and gel states. Cryo-SEM (**a**, **b**) and -TEM (**c**, **d**) images of Swy-3 sodium-montmorillonite in **a**, **b** sol (1.9 wt%) and **b**, **d** gel states (6.6 wt%).

whereas the gel state had regions of particle aggregation along with domains where particles were ordered in a face-face manner (Fig. 6b, d and Supplementary Figure 5). Unlike the plunge frozen technique during Cryo-SEM sample preparation, which produces a honeycomb structure[55,56], the high-pressure technique used here produced no honeycomb pattern. These complementary results confirm the presence of aggregation in Na-Mt suspensions in both sol and gel states. It is worth noting that the interparticle distance measured on cryo-EM images is significantly greater than the interparticle distance (~15 Å) reported for tactoids[57]. Therefore, the nematic character of the gel is attributed to face-face ordering of the Na-Mt particles. Furthermore, the Cryo-TEM results show that both the sol and gel states exhibit ordering with a repeat distance of ~20 nm and ~10 nm, respectively. While the repeat distance results obtained from Cryo-TEM are not directly related to the results obtained from the X-ray scattering experiments, the expected change in sol and gel state is captured. This may be linked to the Cryo-TEM sample preparation procedure which was a little different than the high-pressure Cryo-SEM method where the repeat distances obtained are much closer to the repeat distances obtained using X-ray scattering.

Dilution behaviour. The dilution method used in previous research to distinguish between a repulsive and an attractive system was used here[58,59]. The gel state showed a tendency to melt at all concentrations, with the time required to melt increasing with concentration (Fig. 7). The time required for the gel to melt completely was significantly greater for Na-Mt than for laponite, a synthetic swelling clay[58,59]. Although aggregation in the system was confirmed, the system still melts when in contact with water. This may be linked to the transport characteristics of water inside the gel, which may be related to high-permeability streaks in the gel arising from strongly ordered domains. As a result, water penetrates easily into the structure at lower concentrations since the particles are not tightly packed. At

higher concentrations, particles are closer together, and the structure has lower permeability and porosity.

Discussion

We probed the microstructure of Na-Mt aqueous suspensions covering a length scale of more than five orders from interatomic distances using WAXS and to more than an order larger than the particle size using USAXS and USANS. The scattering profile in the WAXS region remained unaltered as a function of concentration; thus, the microstructure remained unaffected at these length scales. For the SAXS region, the intensity decayed at a rate of ~2, regardless of Na-Mt concentration. Previous work on Na-Mt suspensions covered a length scale up to only a maximum of 100 nm, which is within the particle size range of Na-Mt particles[54,60–63]. Therefore, the presence of Bragg peak in the SAXS region is evidence of a purely repulsive microstructure. Scattering at larger length scales using USAXS showed that the microstructure contains entities larger than ~6 μm, and the aggregation at this length scale only intensified as a function of concentration. USANS further showed that the aggregated entities are larger than 17 μm. Therefore, the presence of scattering objects at a length scale of 17 μm and Bragg peaks in the SAXS region signify the presence of two domains: one has particle-particle aggregation, and the other has particle-particle ordering.

This was further confirmed by cryo-SEM and cryo-TEM images where particle-particle aggregation and particle-particle ordering were visible. The presence of domains was also reflected in dilution behaviour, whereby the gelled structure melted upon contact with water. The time required to melt the gel increased as a function of concentration due to the enhanced gel strength and aggregation as a function of concentration. Therefore, the Bragg peak in the SAXS region only reveals particle-particle ordering from unaggregated domains. Bihannic et al.[18] detected the existence of large-scale structures much larger than individual clay platelets formed by alternating clay-rich and clay-poor domains
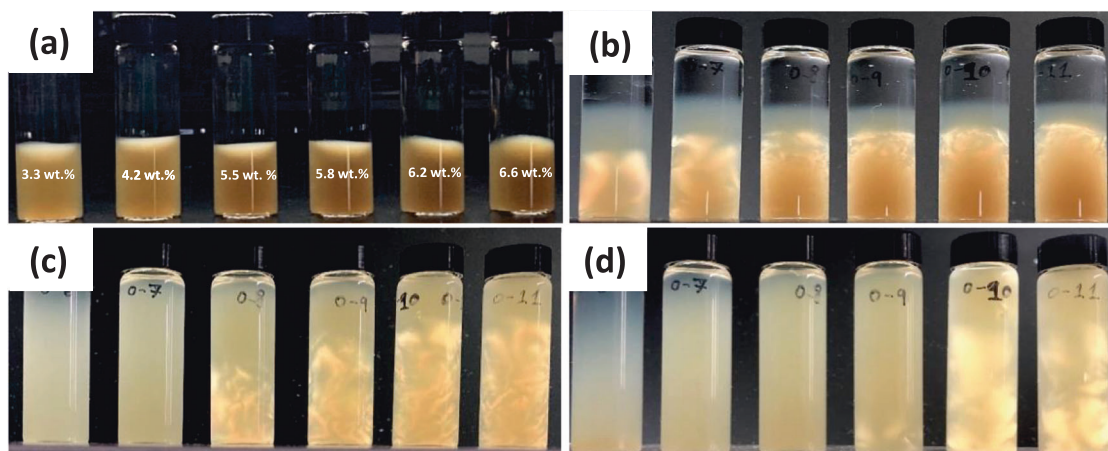
Fig. 7 Dilution/dissolution behavior. Dilution behaviour of Na-Mt suspensions at different concentrations in the gel state after **a** 0, **b** 2, **c** 47, and **d** 150 days.

using synchrotron-based X-ray fluorescence microscopy. However, these authors used osmotically prepared suspensions, and the structure within the domains was not detectable due to the insufficient resolution of the technique.

The fundamental mechanism behind the formation of particle-particle ordering can be understood from Onsager's liquid crystal theory[64]. However, the presence of aggregated domains is perplexing and raises several fundamental questions regarding the mechanisms and properties of gels in systems of charged colloidal platelets. There may be one or a combination of mechanisms responsible for aggregation. Firstly, the Na-Mt particle size distribution is quite broad, and the surface charge characteristics of these particles may vary as a function of particle size range. The larger particle size range may have low-charge regions that can aggregate in a patch-wise manner through alignment of low- or opposite-charge domains (positive facing negative) especially at higher particle concentrations[65,66]. Smaller particles may drive aggregation of larger particles due to depletion[67,68]; this effect may be enhanced if the larger particle size range also has low-charge regions. If this is the case, then suspensions of fractionated Na-Mt particles will have a strong particle-size-dependent microstructure.

Michot et al.[26] reported the effect of particle size on the phase diagram of fractionated Na-Mt suspensions obtained by successive centrifugation. The authors concluded that the effect of anisotropy on Na-Mt suspensions was opposite to that of other systems of charged colloidal platelets, where smaller particles exhibited a sol-gel transition at lower solid concentrations than larger particles. The inverse relationship of sol-gel transition was speculated to be linked to particle-particle association, giving rise to disconnected clusters whose amount increases linearly with decreasing particle size. Such disconnected clusters were speculated to give rise to a heterogeneous suspension, which we have confirmed using scattering and cryo-EM experiments. Ion-ion association effects on the appearance of attraction between equally charged particles in the presence of multivalent ions (e.g., cement cohesion) should also be investigated and may drive the particle-particle aggregation observed here[32,69–71].

Conclusions

The microstructure of a liquid-crystalline clay suspension was probed using USAXS, USANS, and complementary Cryo-electron microscopy and dilution studies. For the first time, the microstructure of these suspensions was studied up to a length scale of 17 μm, which is more than an order of magnitude larger than the largest particle size. Neither of the two models proposed to date for nematic microstructure—a purely jammed suspension stabilized by repulsive electrostatic forces between particles and a percolated network governed by electrostatic attraction between platelets—accurately captures the real microstructure. The scattering results reveal the microstructure contains entities that are at least one order of magnitude larger than the individual particles. They also confirm the presence of domains having particle-particle ordering in the assembly of particles, refuting the purely repulsive nature of these gels. The presence of nematic domains refutes a purely attractive nature. The microstructure can be viewed as a hybrid that has both attractive or aggregated and repulsive or ordered domains.

Methods

Sample preparation. Swy-3 montmorillonite clay was obtained from the Source Clays Minerals Repository of the Clay Mineral Society (Purdue University). The reported cation exchange capacity (CEC) of Swy-3 is around 96 meq per 100 g[12]. The measured BET surface area was 34.02 m^2 per g. The clay sample was purified by settling a 45 gram per Liter suspension of clay in 1 M NaCl in an Imhoff cone for 72 h with three 1 M NaCl exchanges. The bottom fraction of the suspension was discarded, and the top fraction was dialyzed against deionized (DI) water at a water: suspension ratio of 50. The DI water was exchanged several times until the conductivity of the reservoir fell below 5 μS·m^{-1}, and a silver nitrate test confirmed the absence of chloride ions. This procedure resulted in a fully Na$^+$-exchanged montmorillonite at ultra-low ionic strength. The suspension obtained from the dialysis tube was centrifuged at 6300 × g for 90 min to remove coarse particles. The pellet was discarded, and the final stock suspension was collected in a beaker. The weight concentration of stock suspension was obtained by oven-drying a small sample at 120 °C for 48 h. The fractionation procedure used here was intended to just get rid of coarser particles and impurities and didn't result in a pauci-dispersed sample as evident from the size range of particles present (20–632 nm). The final stock suspension was dialyzed in membranes with a molecular weight cut-off of 12,000–14,000 Da.

Osmotic stress experiments were performed with polyethylene glycol (molecular weight 35,000 Da) in DI water at different concentrations to obtain clay suspensions in sol and gel states. Osmotic stress experiments were equilibrated for 30 days, during which time the polymer solution was renewed three times. Final clay suspension concentrations were determined by weight loss
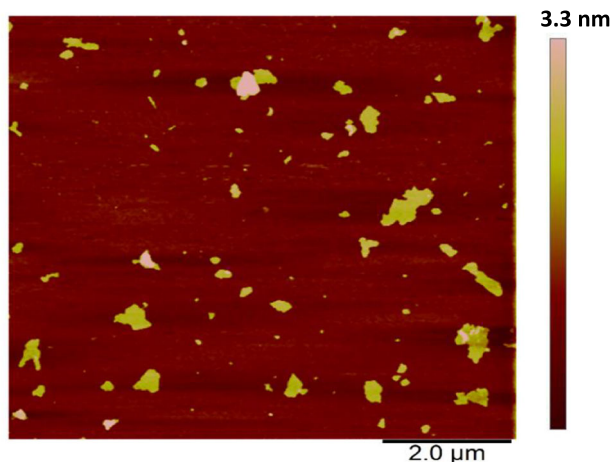
Fig. 8 Atomic force microscopy image of the Na-Mt sample used in the study. Representative atomic force microscopy image of the Na-Mt sample. Mean diameter: 218 ± 127 nm (range 20–632 nm). Mean thickness: 2 ± 0.824 nm (range 0.55–6.7 nm).

upon oven-drying a small fraction of equilibrated suspensions at 120 °C for 48 h. Osmotic pressure values for 35,000 Da polyethylene glycol can be found elsewhere[42].

USANS samples were prepared in D_2O obtained from Sigma Aldrich (Item # 7789-20-0). The dried sample obtained after the centrifugation step was dispersed in D_2O at 0.50 wt% and equilibrated for a month after which the sample was filled in membranes of molecular weight cut-off of 12,000–14,000 Da. A concentrated stock suspension was obtained by applying osmotic stress using 35,000 Da polyethylene glycol in D_2O. The osmotic pressure was increased gradually from 1000 to 8000 Pa by increasing the concentration of polyethylene glycol. The concentrated stock suspension obtained was diluted using D_2O to obtain several concentrations of Na-Mt in D_2O.

Particle size analysis. The maximum particle size of the montmorillonite stock suspension measured with a Nanoparticle Tracking Analysis instrument (NanoSight NSss300, Malvern) by tracking more than 1000 particles (Supplementary Figure 6) was less than 600 nm. Atomic force microscopy was also carried out to determine the size and thickness of purified clay particles. The surfaces of freshly cleaved, high-grade (V-1), 12 mm mica discs (Ted Pella Inc., Redding, CA) were treated for 5 min with 10 μL of 3-aminopropyl-trietoxy silane (1 μM in DI water), rinsed with 2 mL DI water, and blow dried. A 10 μL drop of 0.012 mg per mL montmorillonite suspension was incubated on the mica discs for 5 min in a wet chamber to avoid desiccation. Discs were dried in a laboratory fumehood at room temperature and scanned immediately on a BioScope™ II atomic force microscope (Bruker Corporation, Billerica, MA). High-resolution images of montmorillonite particles were obtained using RTESP cantilevers (fo = 237–289 kHz, k = 20–80 N/m, Bruker Corporation, Billerica, MA) (Fig. 8). The particle nanotopography was determined using the tapping mode in air at a 0.7 Hz scan rate. Particle analysis, size distribution, and three-dimensional images were obtained with NanoScope Analysis© software (Ver. 1.50, Bruker Corporation, Billerica, MA). The particle size range obtained from the two methods was in good agreement with each other.

Rheology. A stress-controlled Discovery HR-2 (TA Instruments) rheometer was used to measure the rheology of Na-Mt suspensions at 25 °C. A concentric cylinder geometry (bob and cylinder wall sandblasted to limit wall slip) was used, with bob and cup diameters of 28 and 30.4 mm, respectively, resulting in a shearing gap of 1.2 mm. A thin layer of silicone oil was applied to the top surface of the suspensions to prevent evaporation during tests. The overall procedure was as follows: (1) pre-shear at $+1500$ s^{-1} and -1500 s^{-1} for 2 min each to minimize the effect of sample loading history; and (2) wait 60 min and then perform the strain amplitude sweep at 1 Hz to obtain the linear viscoelastic region storage modulus (G') (Supplementary Figure 1).

Ultra-small angle X-ray scattering (USAXS). Measurements were carried out at the 9-ID-C beamline of the Advanced Photon Source at Argonne National Laboratory[72]. Samples were placed in 1-mm capillary tubes, which were then sealed. The wavelength (λ) of the incident X-ray was 0.5904 Å (21 keV). The beam size was ≈0.8 (width) × 0.2 (height) mm^2 for SAXS and WAXS and 0.8 (width) × 0.8 (height) mm^2 for USAXS. Each USAXS measurement was acquired for 60 s with a scattering vector, Q (Q = $4\pi\sin\theta\lambda^{-1}$)[73] ranging from 10^{-4} to 6×10^{-1} Å^{-1} with a resolution ≈ 8×10^{-5} Å^{-1}. The SAXS and WAXS data were acquired for 30 s each over Q ranges of 3×10^{-2}–1.3 and 1–7 Å^{-1}, respectively. The background solution (10^{-5} M NaCl in DI water) was subtracted from the main intensities. Data were reduced using the INDRA and NIKA[74] software packages and analyzed using the IRENA software package[75]. Data were also de-smeared from slit-smeared collimation of the Bonse-Hart USAXS system.

Ultra-small angle neutron scattering (USANS). The USANS measurements were performed on the KOOKABURRA[76] beamline at the OPAL reactor (Lucas Heights, NSW, Australia). The USANS measurements were performed to cover a Q-range from 3.5×10^{-5} Å^{-1} to 10^{-2} Å^{-1} using a Bonse-Hart instrument. The samples were loaded into demountable sample cells with a path length of 1 mm. A thermally controlled sample charger was used to control the sample temperature to 25 °C. The experimental USANS data were de-smeared using the Lake algorithm incorporated in NIST USANS macros[77].

Cryo-scanning electron microscopy. Samples were placed in a Leica HMP-100 High-Pressure Freezer and stored in liquid nitrogen before being loaded into a Leica VCT 100 cryo-transfer shuttle and coated with 7 nm of PtC^{-1} and 5 nm of carbon within a Leica ACE 600 high-vacuum sputter coater. After coating, samples were kept frozen and loaded with the shuttle into a Hitachi S4800-II cold field emission gun scanning electron microscope fitted with a Leica cryo-stage and imaged at 5 kV with an approximate working distance of 10 mm. See Supplementary Figure 6.

Cryo-transmission electron microscopy. Samples were vitrified in liquid ethane with a Vitrobot Mark IV (Thermo Scientific). Liquid samples were pipetted onto Quantifoil R2/2 copper grids (Electron Microscopy Sciences) that had been glow-discharged in air (PELCO easiGlow, Ted Pella, Inc.). Gel samples were deposited into the grids by dipping the grid into the gel before blotting and plunge freezing. Grids were transferred into a transmission electron microscope single-tilt cryo-holder (Gatan). Grids were imaged in a Talos L120C (Thermo Scientific) with a high tension of 120 kV with a 4 × 4 k BM-Ceta CMOS camera. At least 50 images of each sample were taken at magnifications of ×28,000, ×57,000, and ×120,000, yielding a pixel size of 510, 249, and 121 pm, respectively.

Dilution studies. Gelled samples (~4.50 g) were transferred to vials to which 7.5 mL DI water was gently added. The water

volume was sufficient to bring the highest concentration from a gel to a sol state once the gel melted completely. The vials were closed and left undisturbed for 150 days. Photographs were taken at 0, 2, 47, and 150 days.

Data availability
All data supporting this study's findings are available within the article and supplementary section. The datasets used and/or analyzed during the current study are available from the corresponding author upon reasonable request.

References
1. Murray, H. H. Overview—clay mineral applications. *Appl. Clay Sci.* **5**, 379–395 (1991).
2. Ho, T. A., Criscenti, L. J. & Greathouse, J. A. Revealing transition states during the hydration of clay minerals. *J. Phys. Chem. Lett.* **10**, 3704–3709 (2019).
3. Jerolmack, D. J. & Daniels, K. E. Viewing Earth's surface as a soft-matter landscape. *Nat. Rev. Phys.* **1**, 716–730 (2019).
4. Ball, P. Shaped from clay. *Nature* https://doi.org/10.1038/news051031-10 (2005).
5. Ferris, J. P. Montmorillonite-catalysed formation of RNA oligomers: the possible role of catalysis in the origins of life. *Philos. Trans. Royal Soc. B: Biol. Sci.* **361**, 1777–1786 (2006).
6. Langmuir, I. The role of attractive and repulsive forces in the formation of tactoids, thixotropic gels, protein crystals and coacervates. *J. Chem. Phys.* **6**, 873–896 (1938).
7. Freundlich, H. *Kolloid-Zeitschrift* Vol. 46, 289–299 (1928).
8. Whittaker, M. L., Lammers, L. N., Carrero, S., Gilbert, B. & Banfield, J. F. Ion exchange selectivity in clay is controlled by nanoscale chemical–mechanical coupling. *Proc. Natl Acad. Sci. USA* **116**, 22052–22057 (2019).
9. Norrish, K. Crystalline swelling of montmorillonite: manner of swelling of montmorillonite. *Nature* **173**, 256–257 (1954).
10. Swartzen-Allen, S. L. & Matijevic, E. Surface and colloid chemistry of clays. *Chem. Rev.* **74**, 385–400 (1974).
11. Norrish, K. & Quirk, J. P. Crystalline swelling of montmorillonite: use of electrolytes to control swelling. *Nature* **173**, 255–256 (1954).
12. Paineau, E. et al. Aqueous suspensions of natural swelling clay minerals. 1. Structure and electrostatic interactions. *Langmuir* **27**, 5562–5573 (2011).
13. Paineau, E. et al. Liquid–crystalline properties of aqueous suspensions of natural clay nanosheets. *Liq. Cryst. Rev.* **1**, 110–126 (2013).
14. Michot, L. J. et al. Isotropic/nematic and sol/gel transitions in aqueous suspensions of size selected nontronite NAu1. *Clay Minerals* **48**, 663–685 (2013).
15. Michot, L. J. et al. Liquid–crystalline aqueous clay suspensions. *Proc. Natl Acad. Sci. USA* **103**, 16101–16104 (2006).
16. Michot, L. J. et al. Sol/Gel and isotropic/nematic transitions in aqueous suspensions of natural nontronite clay. Influence of PArticle Anisotropy. 1. Features of the I/N transition. *Langmuir* **24**, 3127–3139 (2008).
17. Paineau, E. et al. In-situ SAXS study of aqueous clay suspensions submitted to alternating current electric fields. *J. Phys. Chem. B* **116**, 13516–13524 (2012).
18. Bihannic, I. et al. First direct visualization of oriented mesostructures in clay gels by synchrotron-based X-ray fluorescence microscopy. *Langmuir* **17**, 4144–4147 (2001).
19. Davidson, P. & Gabriel, J.-C. P. Mineral liquid crystals. *Curr. Opin. Colloid Interface Sci.* **9**, 377–383 (2005).
20. Mourad, M. C. D., Wijnhoven, J. E. G. J., van 't Zand, D. D., van der Beek, D. & Lekkerkerker, H. N. W. Gelation versus liquid crystal phase transitions in suspensions of plate-like particles. *Philos. Trans. Royal Soc. A: Math. Phys. Eng. Sci.* **364**, 2807–2816 (2006).
21. Norrish, K. The swelling of montmorillonite. *Disc. Faraday Soc.* **18**, 120–134 (1954).
22. Callaghan, I. C. & Ottewill, R. H. Interparticle forces in montmorillonite gels. *Faraday Disc. Chem. Soc.* **57**, 110–118 (1974).
23. Abend, S. & Lagaly, G. Sol–gel transitions of sodium montmorillonite dispersions. *Appl. Clay Sci.* **16**, 201–227 (2000).
24. Sposito, G. & Prost, R. Structure of water adsorbed on smectites. *Chem. Rev.* **82**, 553–573 (1982).
25. Shalkevich, A., Stradner, A., Bhat, S. K., Muller, F. & Schurtenberger, P. Cluster, glass, and gel formation and viscoelastic phase separation in aqueous clay suspensions. *Langmuir* **23**, 3570–3580 (2007).
26. Michot, L. J. et al. Phase diagrams of wyoming Na-montmorillonite clay. Influence of particle anisotropy. *Langmuir* **20**, 10829–10837 (2004).
27. Van Olphen, H. Rheological phenomena of clay sols in connection with the charge distribution on the micelles. *Disc. Faraday Soc.* **11**, 82–84 (1951).
28. Morvan, M., Espinat, D., Lambard, J. & Zemb, T. Ultrasmall- and small-angle X-ray scattering of smectite clay suspensions. *Colloids Surf. A: Physicochem. Eng. Asp.* **82**, 193–203 (1994).
29. Baravian, C., Vantelon, D. & Thomas, F. Rheological determination of interaction potential energy for aqueous clay suspensions. *Langmuir* **19**, 8109–8114 (2003).
30. Mourchid, A., Lécolier, E., Van Damme, H. & Levitz, P. On viscoelastic, birefringent, and swelling properties of laponite clay suspensions: revisited phase diagram. *Langmuir* **14**, 4718–4723 (1998).
31. Michot, L. J. et al. Sol−Gel and isotropic/nematic transitions in aqueous suspensions of natural nontronite clay. Influence of particle anisotropy. 2. Gel structure and mechanical properties. *Langmuir* **25**, 127–139 (2009).
32. Goyal, A. et al. The physics of cement cohesion. *Sci. Adv.* **7**, eabg5882 (2021).
33. Plassard, C., Lesniewska, E., Pochard, I. & Nonat, A. Nanoscale experimental investigation of particle interactions at the origin of the cohesion of cement. *Langmuir* **21**, 7263–7270 (2005).
34. Bailey, L., Lekkerkerker, H. N. W. & Maitland, G. C. Smectite clay – inorganic nanoparticle mixed suspensions: phase behaviour and rheology. *Soft Matter* **11**, 222–236 (2015).
35. McBride, M. B. & Baveye, P. Diffuse double-layer models, long-range forces, and ordering in clay colloids. *Soil Sci. Soc. Am. J.* **66**, 1207–1217 (2002).
36. Quirk, J. P. Comments on "Diffuse double-layer models, long-range forces, and ordering of clay colloids". *Soil Sci. Soc. Am. J.* **67**, 1960–1961 (2003).
37. Quirk, J. P. In *Advances in Agronomy* (ed. Sparks, D. L.) Vol. 53, 121–183 (Academic Press, 1994).
38. Overbeek, J. T. G. On the interaction of highly charged plates in an electrolyte: a correction. *Mol. Phys.* **80**, 685–694 (1993).
39. Smalley, M. V. & Sogami, I. S. On the interaction of highly charged plates in an electrolyte. *Mol. Phys.* **85**, 869–881 (1995).
40. Batista, C. A. S., Larson, R. G. & Kotov, N. A. Nonadditivity of nanoparticle interactions. *Science* **350**, 1242477 (2015).
41. Ilavsky, J. et al. Ultra-small-angle X-ray scattering at the advanced photon source. *J. Appl. Crystallogr.* **42**, 469–479 (2009).
42. Jönsson, B., Persello, J., Li, J. & Cabane, B. Equation of state of colloidal dispersions. *Langmuir* **27**, 6606–6614 (2011).
43. Bonnet-Gonnet, C., Belloni, L. & Cabane, B. Osmotic pressure of latex dispersions. *Langmuir* **10**, 4012–4021 (1994).
44. Calabrese, V., Haward, S. J. & Shen, A. Q. Effects of shearing and extensional flows on the alignment of colloidal rods. *Macromolecules* **54**, 4176–4185 (2021).
45. Tudisca, V., Ricci, M. A., Angelini, R. & Ruzicka, B. Isotopic effect on the aging dynamics of a charged colloidal system. *RSC Advances* **2**, 11111–11116 (2012).
46. Mourad, M. C. D. et al. Sol−Gel transitions and liquid crystal phase transitions in concentrated aqueous suspensions of colloidal gibbsite platelets. *J. Phys. Chem. B* **113**, 11604–11613 (2009).
47. Michot, L. J. et al. Coagulation of Na-montmorillonite by inorganic cations at neutral pH. A combined transmission X-ray microscopy, small angle and wide angle X-ray scattering study. *Langmuir* **29**, 3500–3510 (2013).
48. Murphy, R. P., Hong, K. & Wagner, N. J. Thermoreversible gels composed of colloidal silica rods with short-range attractions. *Langmuir* **32**, 8424–8435 (2016).
49. Kishore, S., Srivastava, S. & Bhatia, S. R. Microstructure of colloid-polymer mixtures containing charged colloidal disks and weakly-adsorbing polymers. *Polymer* **105**, 461–471 (2016).
50. Bhatia, S. R. Ultra-small-angle scattering studies of complex fluids. *Curr. Opin. Colloid Interface Sci.* **9**, 404–411 (2005).
51. Dimon, P. et al. Structure of aggregated gold colloids. *Phys. Rev. Lett.* **57**, 595–598 (1986).
52. Shan, L., Xie, R., Wagner, N. J., He, H. & Liu, Y. Microstructure of neat and SBS modified asphalt binder by small-angle neutron scattering. *Fuel* **253**, 1589–1596 (2019).
53. Gabriel, J.-C. P. et al. Swollen liquid-crystalline lamellar phase based on extended solid-like sheets. *Nature* **413**, 504–508 (2001).
54. Segad, M., Cabane, B. & Jönsson, B. Reactivity, swelling and aggregation of mixed-size silicate nanoplatelets. *Nanoscale* **7**, 16290–16297 (2015).
55. Mouzon, J., Bhuiyan, I. U. & Hedlund, J. The structure of montmorillonite gels revealed by sequential cryo-XHR-SEM imaging. *J. Colloid Interface Sci.* **465**, 58–66 (2016).
56. Deirieh, A. et al. Particle arrangements in clay slurries: the case against the honeycomb structure. *Appl. Clay Sci.* **152**, 166–172 (2018).
57. Hotton, C. et al. Organisation of clay nanoplatelets in a polyelectrolyte-based hydrogel. *J. Colloid Interface Sci.* **604**, 358–367 (2021).

58. Ruzicka, B. et al. Competing interactions in arrested states of colloidal clays. *Phys. Rev. Lett.* **104**, 085701 (2010).

59. Angelini, R. et al. Glass–glass transition during aging of a colloidal clay. *Nat. Commun.* **5**, 4049 (2014).

60. Ramsay, J. D., Swanton, S. W. & Bunce, J. Swelling and dispersion of smectite clay colloids: determination of structure by neutron diffraction and small-angle neutron scattering. *J. Chem. Soc., Faraday Trans.* **86**, 3919–3926 (1990).

61. Segad, M. et al. Microstructural and swelling properties of Ca and Na montmorillonite: (in situ) observations with cryo-TEM and SAXS. *J. Phys. Chem. C* **116**, 7596–7601 (2012).

62. Segad, M., Jönsson, B. & Cabane, B. Tactoid formation in montmorillonite. *J. Phys. Chem. C* **116**, 25425–25433 (2012).

63. Ramsay, J. D. F. & Lindner, P. Small-angle neutron scattering investigations of the structure of thixotropic dispersions of smectite clay colloids. *J. Chem. Soc., Faraday Trans.* **89**, 4207–4214 (1993).

64. Lekkerkerker, H. N. W. & Vroege, G. J. Liquid crystal phase transitions in suspensions of mineral colloids: new life from old roots. *Philos. Trans. Royal Soc. A: Math. Phys. Eng. Sci.* **371**, 20120263 (2013).

65. Silbert, G. et al. Long-ranged attraction between disordered heterogeneous surfaces. *Phys. Rev. Lett.* **109**, 168305 (2012).

66. Adar, R. M., Andelman, D. & Diamant, H. Electrostatics of patchy surfaces. *Adv. Colloid Interface Sci.* **247**, 198–207 (2017).

67. Lekkerkerker, H. N. W.& Tuinier, R. In *Colloids and the Depletion Interaction* 57–108 (Springer Netherlands, 2011).

68. Lekkerkerker, H. & Tuinier, R. *Colloids and the Depletion Interaction* 233 (2011).

69. Shen, X. & Bourg, I. C. Molecular dynamics simulations of the colloidal interaction between smectite clay nanoparticles in liquid water. *J. Colloid Interface Sci.* **584**, 610–621 (2021).

70. French, R. H. et al. Long range interactions in nanoscale science. *Rev. Mod. Phys.* **82**, 1887–1944 (2010).

71. Jellander, R., Marčelja, S. & Quirk, J. P. Attractive double-layer interactions between calcium clay particles. *J. Colloid Interface Sci.* **126**, 194–211 (1988).

72. Ilavsky, J. et al. Development of combined microstructure and structure characterization facility for in situ and operando studies at the Advanced Photon Source. *J. Appl. Crystallogr.* **51**, 867–882 (2018).

73. Li, T., Senesi, A. J. & Lee, B. Small angle X-ray scattering for nanoparticle research. *Chem. Revi.* **116**, 11128–11180 (2016).

74. Ilavsky, J. Nika: software for two-dimensional data reduction. *J. Appl. Crystallogr.* **45**, 324–328 (2012).

75. Ilavsky, J. & Jemian, P. R. Irena: tool suite for modeling and analysis of small-angle scattering. *J. Appl. Crystallogr.* **42**, 347–353 (2009).

76. Rehm, C., Brule, A., Freund, A. K. & Kennedy, S. J. Kookaburra: the ultra-small-angle neutron scattering instrument at OPAL. *J. Appl. Crystallogr.* **46**, 1699–1704 (2013).

77. Kline, S. Reduction and analysis of SANS and USANS data using IGOR Pro. *J. Appl. Crystallogr.* **39**, 895–900 (2006).

Acknowledgements

Author contributions

M.S. conceived the conceptual idea and devised the research plan. E.R.B. acquired the funding, supervised the research, and reviewed the manuscript. M.S. executed the experiment, and data analysis and wrote the manuscript. S.K. and O.B.W. assisted in sample preparation and reviewing the manuscript. J.M., A.J.K., I.K., and M.B. assisted in the scattering experiments and data interpretation. L.K.F. and E.W.R. assisted in electron microscopy experiments and data analysis.

Competing interests

The authors declare no competing interests.

Additional information

Supplementary information The online version contains supplementary material available at https://doi.org/10.1038/s43246-023-00414-y.

Correspondence and requests for materials should be addressed to Mohammad Shoaib or Erin R. Bobicki.

Peer review information *Communications Materials* thanks Will Gates, Frédéric Pignon and Erwan Paineau for their contribution to the peer review of this work. Primary Handling Editors: Jet-Sing Lee and John Plummer. A peer review file is available

Reprints and permission information is available at http://www.nature.com/reprints

Publisher's note Springer Nature remains neutral with regard to jurisdictional claims in published maps and institutional affiliations.